IEEE Access
Multidisciplinary | Rapid Review | Open Access Journal

Received February 14, 2020, accepted March 11, 2020, date of publication March 30, 2020, date of current version June 9, 2020.

Digital Object Identifier 10.1109/ACCESS.2020.2984424

Active Modeling and Compensation for the Hysteresis of a Robotic Flexible Ureteroscopy

XIANGYU WANG, (Student Member, IEEE), DONGYANG BIE, JIANDA HAN, (Member, IEEE), AND YONGCHUN FANG, (Senior Member, IEEE)

College of Artificial Intelligence, Institute of Robotics and Automatic Information Systems, Nankai University, Tianjin 300000, China

Corresponding author: Jianda Han (hanjianda@nankai.edu.cn)

ABSTRACT Hysteresis may be one of the most critical issues degrading the performance of the automatic operation of robotic flexible ureteroscopy, i.e., a robotic device handles the flexible ureteroscopy tracking a target automatically. In this paper, we proposed an active-model based scheme to estimate the hysteresis in real time. Firstly, we used the Coleman-Hodgdon model to describe the backlash hysteresis property of the flexible scope, and constructed the reference model of the bending angle. Secondly, a modeling error was introduced into the reference model, and the UKF-based estimator was used to estimate both the bending angle and the modeling error actively. Finally, we designed the hysteresis compensation based on this active estimation enhanced model. Extensive experiments were conducted on the self-built robotic ureteroscopy. The experimental results with the active modeling enhancement were presented and compared with those without it, to demonstrate the improvements achieved by the proposed scheme.

INDEX TERMS Active model-based control, model error, hysteresis compensation, soft robot, surgery robot.

I. INTRODUCTION

Besides the minimal invasive surgery (MIS), the natural orifice transluminal endoscopic surgery (NOTES) has been developing rapidly in the last decades [1]–[4]. Compared to the open surgery, both NOTES and MIS have decreased surgical morbidity and postoperative recovery time benefited from the smaller or even no incision [5]. However, there are still difficulties while the doctors performing NOTES operations, and how to accurately navigate and locate the flexible endoscope inside the ''closed'' human organs may be one of the most significant challenges.

As shown in Fig. 1, flexible ureteroscope based operation, namely, ureteroscopy, is one of the most popular NOTES that is being adopted by more and more patients and doctors. A flexible ureteroscope is an instrument that is used to pass through and see inside of the urinary tract. Usually, it is used in ureteroscopies to locate and shatter kidney stones. During the ureteroscopy, a ureteral access sheath is first inserted into the urethra, then the surgeon will operate the flexible ureteroscope passing the sheath into the bladder and then the ureter and finally the kidneys. This procedure doesn't require an incision, making it less invasive and reducing the risk of infection for the patient.

As Fig. 2 shows, normally there are 3 controllable degree-of-freedoms (DOFs) on a flexible ureteroscope, namely back-and-forth of ξ, rotation of β and tip-bending of α, which can be operated via the handle shown in Fig. 2. The tip-bending of the ureteroscope is driven by a very thin and solid wire going through the scope's epidermis and fixed on the two rings of the handle. When the wire is pulled by the surgeon, the tip-part will bend correspondingly; On the contrary, when the wire is loosened, the tip-part will straighten. During ureteroscopies, the surgeon operates the 3-DOFs and focuses the scope tip on the target point, a small stone in kidney for example. Actually, it is not easy for a surgeon to control the flexible scope and locate its tip accurately on the target.

Instead of a surgeon, a robotic device can also be constructed to operate the 3 DOFs of the scope via the handle, while the surgeon controls the robot remotely [6]. However, a master-slave-type robotic system also depends on human surgeon's experiences for the accurate allocation of the scope tip. In order to make the robot focus on the target point automatically, we have to develop a kinematic model of the flexible ureteroscope, and the accuracy of the tip allocation will closely depend on the accuracy of the kinematics [7].

The associate editor coordinating the review of this manuscript and approving it for publication was Okyay Kaynak.

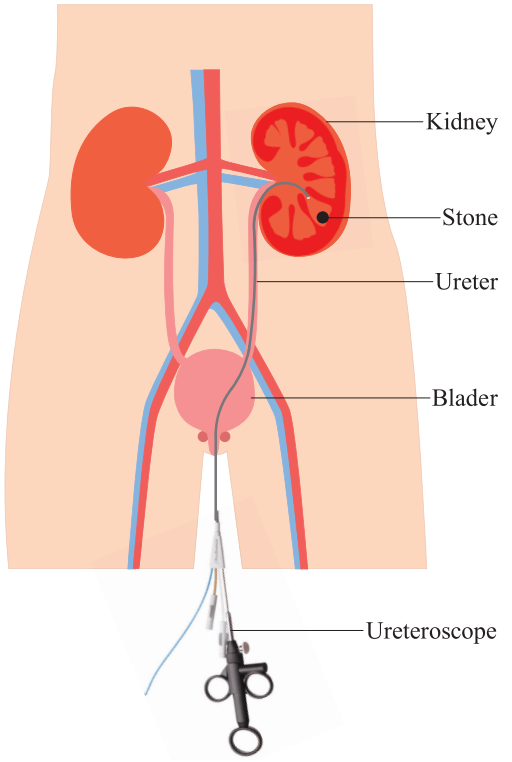

FIGURE 1. The diagram of the ureteroscopic lithotripsy to treat kidney stone.

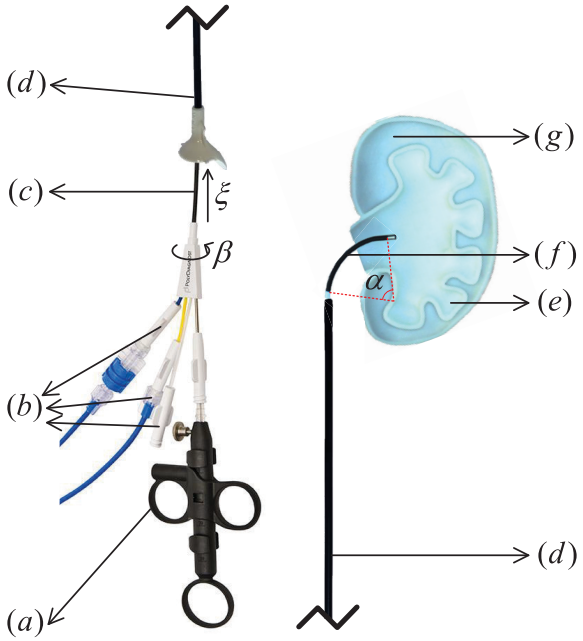

FIGURE 2. The illustration of the ureteroscope and kidney model: (a) the pull-ring of the ureteroscope, (b) the accesses for other medical instruments, (c) the flexible part of the ureteroscope, (d) the ureteral access sheath (from COOK ® MEDICAL) where the ureteroscope goes through, (e) the renal pelvis of the kidney where the stones usually appear, (f) the bending part (tip-part) of the ureteroscope, (g) the kidney.

Various model identification methods of continuum robots have been carried out in the studies [8]–[10]. Compared with the traditional rigid-link robots, cable-driven continuum surgery robots have hysteresis, elasticity and other nonlinear properties which are difficult to be modeled. The uncertainties of cable-driven robot were analyzed by the tendon-sheath mechanism (TSM) in [11], [12], where static models were proposed at both sliding and pre-sliding regimes to predict the nonlinear hysteresis of TSM. In [13], the ''dead zone'' was analyzed with respect to the friction between tendon and sheath, where the hysteresis of the friction and position was respectively modeled in the form of Bouc-Wen and Coleman-Hodgdon. About the kinematics of flexible scope, Zhang *et al.* approximated the bending angle of ureteroscope into piecewise function [14]–[16], and two curves of flexion angle corresponding to the bi-directional bending knob angle were given out. These two curves were respectively divided into 3 and 5 segments, and a series of linear models were obtained by fitting each segment of the curves into a strain line. Similarly, the studies carried in [17] also used a static model with linearization. But the linearization, as well as the uncaptured uncertainties, might degrade the accuracy of the kinematic model.

In this paper, we proposed an active modeling technique for the flexible ureteroscope. We used the continuous backlash-like hysteresis model, namely, Coleman-Hodgdon model [18], to describe the hysteresis of flexible ureteroscope, and constructed the kinematic model based on the Denavit Hartenberg (D-H) method. The parameters inside this model were identified offline by the experimental data with respect to a specific motion state. Unscented Kalman Filter (UKF) was then used to actively estimated the hysteresis and other modeling errors that did not include in the identified reference model [19]. Finally, an active model enhanced PD controller (AME-PD) was designed to control the bending angle of the ureteroscope tracking a given trajectory.

The main contributions of this paper are summarized as follows:

- The active modeling scheme, which composed of a normal D-H based offline reference model and an active estimation of modeling error, was proposed for the flexible ureteroscope.
- The Unscented Kalman Filter was used as the active estimator in the proposed scheme. An active model enhanced PD controller was also designed to control the tip-part's bending angle tracking a given trajectory automatically.
- Extensive experiments were conducted on a robotic ureteroscope testbed. The experimental results were compared with those without the active estimation, to demonstrate the achievements obtained by the proposed scheme.
- Without losing the generality, the proposed scheme might provide a feasible way for the active modeling and tip-tracking control of other flexible scopes, to decrease the dependency of a surgery robot on the remote control of surgeons.

The rest of this paper is organized as follows. In Section II, a novel kinematic model to describe the hysteresis of the

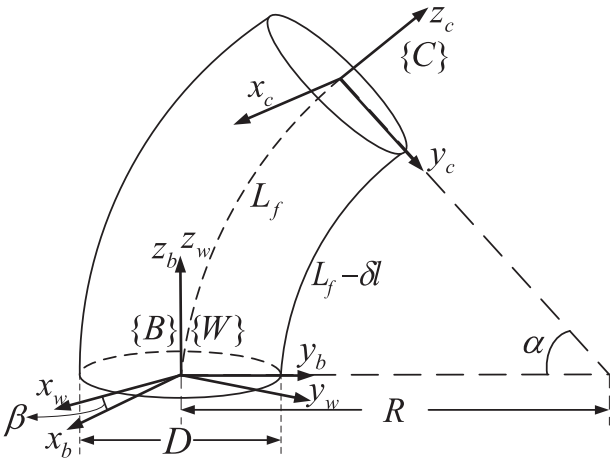

FIGURE 3. The geometric model of ureteroscope's tip.

ureteroscope's tip-part is established. The UKF estimator is designed and the active modeling technology is described in Section III, and the tracking control strategy is proposed in Section IV. Finally, the experimental results were presented and analyzed in Section V, following the conclusion in Section VI.

II. KINEMATICS OF FLEXIBLE URETEROSCOPE

A. GEOMETRIC STRUCTURE AND KINEMATICS

The geometric structure of the ureteroscope is shown in Fig. 3 and the symbol definitions are introduced in Table 1. Here, we assume that the bending part will always be a circular arc.

Thus, the geometric structure of the ureteroscope tip can be described by Fig.3, and we have

$$t_{b\to c} = \begin{bmatrix} 0 \\ \frac{L_f}{\alpha}(1-\cos\alpha) \\ \frac{L_f}{\alpha}\sin\alpha \end{bmatrix} \tag{1}$$

and

$${}^{W}R_B = R_Z(\beta) = \begin{bmatrix} \cos\beta & -\sin\beta & 0 \\ \sin\beta & \cos\beta & 0 \\ 0 & 0 & 1 \end{bmatrix} \tag{2}$$

where ${}^{W}R_B$ represents the rotation transformation of frame {B} rotating clockwise β about the frame {W}. The homogeneous transformation $t_{w\to c}$ can be obtained from (1), (2) as follows

$$\begin{aligned} t_{w\to c} &= {}^{W}R_B t_{b\to c} + t_{w\to b} \\ &= \begin{bmatrix} \cos\beta & -\sin\beta & 0 \\ \sin\beta & \cos\beta & 0 \\ 0 & 0 & 1 \end{bmatrix} \begin{bmatrix} 0 \\ \frac{L_f}{\alpha}(1-\cos\alpha) \\ \frac{L_f}{\alpha}\sin\alpha \end{bmatrix} + \begin{bmatrix} 0 \\ 0 \\ \xi \end{bmatrix} \\ &= \begin{bmatrix} -\sin\beta\frac{L_f}{\alpha}(1-\cos\alpha) \\ \cos\beta\frac{L_f}{\alpha}(1-\cos\alpha) \\ \frac{L_f}{\alpha}\sin\alpha + \xi \end{bmatrix} \end{aligned} \tag{3}$$

where $t_{w\to b} = [0,\ 0,\ \xi]^T$ is the translation transformation of the frame {B} in the frame of {W}. Define the forward kinematic as

$${}^{W}V_C = J_\Phi \dot{\Phi} \tag{4}$$

where

$$\dot{\Phi} = J_\Psi \dot{\Psi} = \begin{bmatrix} \dot{\alpha} \\ \dot{\beta} \\ \dot{\xi} \end{bmatrix} \tag{5}$$

and with the geometric structure, we have

$$\frac{L_f - \delta l}{R - \frac{D}{2}} = \frac{L_f}{R} \tag{6}$$

TABLE 1. Nomenclature and symbols in Fig.3 and equation.

L_f	Length of the ureteroscope's bending part
D	Diameter of the ureteroscope's bending part
R	Radius of the circular arc
α, β, ξ	Bending angle, yawing angle and advanced distance of the ureteroscope's bending part
δl	Pulling distance of the wire
$t_{b\to c}$	Position vector of {C} in the frame of {B}, the rest remains the same
${}^{B}R_C$	Transformation matrix from coordinate system {C} to {B}, the rest remains the same
$R_Z(\beta)$	Transformation matrix of rotating β around the Z axis, the rest remains the same
J_Φ, J_Ψ	Jacobian matrix
Φ, Ψ	State vectors of the tip of the ureteroscope, $\Phi = J_\Psi \Psi$, $\Psi = [\alpha, \beta, \xi]^T$
$\tilde{\alpha}$	Actual value of α by measurement, the rest remains the same
$\hat{\alpha}$	Estimation of α, the rest remains the same
$\bar{\alpha}, \bar{\delta l}, \bar{\tilde{\alpha}}$	Phase transition results of α, δl and $\tilde{\alpha}$, the rest remains the same
$\dot{\alpha}$	The fist derivative of α with respect to time, the rest remains the same
$v_{\delta l}$	Velocity of the pull-ring

thus the translation J_Ψ can be expressed as

$$J_\Psi = \begin{bmatrix} \frac{2}{D} & 0 & 0 \\ 0 & 1 & 0 \\ 0 & 0 & 1 \end{bmatrix}, \dot{\Psi} = \begin{bmatrix} \dot{\delta l} \\ \dot{\beta} \\ \dot{\xi} \end{bmatrix} \tag{7}$$

The kinematic model can be obtained by differentiating position vector $t_{w\to c}$ with respect to time t as follows

$$\begin{aligned} {}^{W}V_C &= \frac{\partial t_{w\to c}}{\partial t} \\ &= J_\xi \dot{\xi} + J_\alpha \dot{\alpha} + J_\beta \dot{\beta} \\ &= J_\Phi \dot{\Phi} \end{aligned} \tag{8}$$

where

$$\begin{aligned} J_\alpha &= \begin{bmatrix} \sin\beta \frac{L_f}{\alpha^2}(1-\cos\alpha) - \sin\beta \frac{L_f}{\alpha}\sin\alpha \\ -\cos\beta \frac{L_f}{\alpha^2}(1-\cos\alpha) + \cos\beta \frac{L_f}{\alpha}\sin\alpha \\ -\frac{L_f}{\alpha^2}\sin\alpha + \frac{L_f}{\alpha}\cos\alpha \end{bmatrix} \\ J_\beta &= \begin{bmatrix} -\cos\beta \frac{L_f}{\alpha}(1-\cos\alpha) \\ -\sin\beta \frac{L_f}{\alpha}(1-\cos\alpha) \\ 0 \end{bmatrix} \quad J_\xi = \begin{bmatrix} 0 \\ 0 \\ 1 \end{bmatrix} \\ J_\Phi &= \begin{bmatrix} J_\alpha & J_\beta & J_\xi \end{bmatrix} \end{aligned} \tag{9}$$

Thus, we get the kinematic model of the ureteroscope as (8).

B. BACKLASH HYSTERESIS MODEL

We could identify the parameters in (8) offline by the measurements with respect to a specific motion state. However, we have seen in our experiments that the output of (8) did not meet the real states accurately (see Fig. 6 of the experimental results). This is mainly due to the hysteresis. The backlash hysteresis nonlinearity of the bending angle of tip-part is due to nonlinear friction of the wire and the elasticity of the ureteroscope. For positive velocity, the bending angle α increases with the pulling distance δl. In the transition phase, the output keeps its previous value at the transition phase. To capture such a backlash hysteresis phenomena of the flexible ureteroscope, a continuous Coleman-Hodgdon model is used. This model describe a standard backlash hysteresis nonlinearity, as written by

$$\dot{\alpha}(t) = A|v_{\delta l}(t)|(C\bar{\delta l}(t) - \bar{\alpha}(t)) + Bv_{\delta l}(t) \tag{10}$$

where the parameters A, B and C are respectively constant coefficient and must satisfy $A > 0, B < 0, C > 0$; $v_{\delta l}(t) = \dot{\delta l}(t)$; $\alpha(t)$, δl is the model value of bending angle and pulling distance, and we have

$$\begin{aligned} \bar{\alpha}(t) &= \alpha(t) - O_\alpha \\ \bar{\delta l}(t) &= \delta l(t) - O_{\delta l} \end{aligned} \tag{11}$$

where the point $O_{Backlash} = (O_{\delta l}, O_\alpha)$ is the origin point of backlash phase, which is the central point of the hysteresis loop in the phase of kinematic. $\bar{\delta l}(t)$ and $\bar{\alpha}(t)$ are the phase transitions of $\delta l(t)$, $\alpha(t)$ respectively.

By (10), the backlash hysteresis of the bending angle α in model (8) is described. This hysteresis model has static parameters and a fixed hysteresis loop. The property of the relation between the input $\delta l(t)$ and output $\alpha(t)$ is that they are monotonically increasing and decreasing between the two extrema. A large value of A or a small value of B means that the hysteresis loop is slim. The hysteresis loop has a steep inclination, when C is large.

III. ACTIVE ESTIMATION OF MODELING ERROR

The hysteresis model of (10) is static with constant parameters, and its accuracy may be degraded by the time-varying uncertainties of the real flexible scope. In order to handle this, we propose in this section a modeling error to describe the uncertainties in (10), and use the unscented Kalman filter to estimate it actively. Thus, we re-write (10) as

$$\begin{cases} \dot{\alpha}(t) = A|v_{\delta l}(t)|(C\bar{\delta l}(t) - \bar{\alpha}(t)) + Bv_{\delta l}(t) + U(t) \\ Y(t) = \alpha(t) + V(t) \end{cases} \tag{12}$$

where $Y(t)$ is the system output which is measurable, $U(t)$ is the process noise involved in the model error and $V(t)$ is the observation noise from the system. All the uncertainties in (12) caused by model error can be considered as additive process noise. Thus, when $v_{\delta l}(t) = 0$, the modeling errors of (12) can be modeled by

$$\begin{cases} f_h(t) = \dot{\tilde{\alpha}}(t) - \dot{\alpha}(t) \\ \dot{f}_h(t) = \vec{0} + h(t) \end{cases} \tag{13}$$

where $f_h(t) \in \mathbb{R}$ represents the model error, $\alpha(t)$ is the state of the reference model (10), $\tilde{\alpha}(t)$ is the actual state, $h(t)$ is assumed to be the process noise actuating the model errors to update, the actual model is defined as

$$\begin{cases} \dot{\tilde{\alpha}}(t) = A|v_{\delta l}(t)|(C\bar{\delta l}(t) - \bar{\tilde{\alpha}}(t)) + Bv_{\delta l}(t) + f_h(t) + U(t) \\ \dot{\alpha}(t) = A|v_{\delta l}(t)|(C\bar{\delta l}(t) - \bar{\alpha}(t)) + Bv_{\delta l}(t) + U(t) \\ \dot{f}_h(t) = h(t) \\ \tilde{Y}(t) = \tilde{\alpha}(t) + V(t) \end{cases} \tag{14}$$

here $\tilde{\alpha}(t)$ represents the measurement of bending angel and $\bar{\tilde{\alpha}}(t) = \tilde{\alpha}(t) - O_\alpha$. Compared with the system's sampling frequency (often 50 Hz or higher), model error $f_h(t)$ can be considered as a slowly time-varying value, and

$$f_{h(k+1)} = f_{h(k)} + h_k \tag{15}$$

Then the discrete description of equation (14) is

$$\begin{cases} \tilde{\alpha}_{k+1} = \tilde{\alpha}_k + [A|v_{\delta l(k)}|(C\bar{\delta l}_k - \bar{\tilde{\alpha}}_k) + Bv_{\delta l(k)} + f_{h(k)}]T_s \\ \quad + U_k \\ f_{h(k)} = f_{h(k)} + h_k \\ \tilde{Y}_k = \tilde{\alpha}_k + V_k \end{cases} \tag{16}$$

where $v_{\delta l(k)} = (\delta l_k - \delta l_{k-1})/T_s$ is the discrete expression of pulling velocity; T_s is the sampling time; $\{\bar{\delta l}_k, \tilde{\alpha}_k, \bar{\tilde{\alpha}}_k, \alpha_k, \bar{\alpha}_k, f_{h(k)}\}$ is the discrete expression of

$\{\bar{\delta l}(t), \tilde{\alpha}(t), \bar{\tilde{\alpha}}(t), \alpha(t), \bar{\alpha}(t), f_h(t)\}$; U_k, V_k are sampling value of $U(t)$, $V(t)$. The discrete state vector is

$$X_k = [\tilde{\alpha}_k \, f_{h(k)}]^T \tag{17}$$

In consideration of the nonlinearity and coupling of model (15), an UKF is used as an estimator to estimate state X_k in real time based on the state-space equation (16). The estimator is designed as

$$\begin{cases} L \cdot L^T = P_{k-1|k-1} \\ \Sigma_{k-1} = [X_{k-1} \ldots X_{k-1}]_{n\times(2n+1)} - [0_{n\times 1} \; -L \; L] \\ \Sigma_{k|k-1}(1,i) = \Sigma_{k-1}(1,i) + T_s[A|v_{\delta l(k)}|(C\bar{\delta l}_k - \\ \quad \Sigma_{k-1}(1,i) + O_\alpha) + Bv_{\delta l(k)} + \Sigma_{k-1}(2,i)] \\ \Sigma_{k|k-1}(2,i) = \Sigma_{k-1}(2,i) \\ P_{X(k|k-1)} = \sum_{i=1}^{2n+1}[W_c(i)(\Sigma_{k|k-1}(i) - W_m\Sigma_{k|k-1}) \\ \quad (\Sigma_{k|k-1}(i) - W_m\Sigma_{k|k-1})^T] + Q_k \\ P_{Y(k|k-1)} = \sum_{i=1}^{2n+1}[W_c(i)(Y_{\Sigma(k|k-1)}(i) - W_m Y_{\Sigma(k|k-1)}) \\ \quad (Y_{\Sigma(k|k-1)}(i) - W_m Y_{\Sigma(k|k-1)})^T] + R_k \\ P_{XY(k|k-1)} = \sum_{i=1}^{2n+1}[W_c(i)(\Sigma_{k|k-1}(i) - W_m\Sigma_{k|k-1}) \\ \quad (Y_{\Sigma(k|k-1)}(i) - W_m Y_{\Sigma(k|k-1)})^T] \\ K_k = P_{XY(k|k-1)}P_{Y(k|k-1)}^{-1} \\ X_{k|k} = W_m\Sigma_{k|k-1} + K_k(Y_k - W_m\Sigma_{k-1}) \\ P_{k|k} = P_{X(k|k-1)} - K_k \cdot P_{XY(k|k-1)}^T \end{cases} \tag{18}$$

wherein Q_k is the covariance matrix of process noise $[U_k, h_k]$, R_k is the covariance matrix of measurement noise V_k, Σ_{k-1} is the confidence field of the state vector X_{k-1}, it is related to the Cholesky decomposition matrix L of confidence matrix P_{k-1}, $X_{k|k}$ is the estimation of state vector based on confidence field $\Sigma_{k|k-1}$, $P_{k|k}$ is the update of confidence matrix $P_{k-1|k-1}$. $\Sigma_{k-1}(i)$, $\Sigma_{k|k-1}(i)$ represents the i-th column vector of Σ_{k-1}, $\Sigma_{k|k-1}$. $\Sigma_{k|k-1}(i,j)$, $\Sigma_{k-1}(i,j)$ means the element at (i,j) of the matrix $\Sigma_{k|k-1}$, Σ_{k-1}, constant n is the dimension of the state vector X_k.

Thus, we can estimate $X_{k|k}$ from (18) and obtain the estimation of both the $\tilde{\alpha}_k$ and $f_{h(k)}$ of (17).

IV. TRACKING CONTROL

The scheme of tracking control is described in Fig. 4. A reference model of the scope needs to be selected and identified first, and then a nominal controller needs to be designed based on this reference model. The system state is estimated in real time by the active modeling technology and input into the compensation strategy unit, which generates the compensation to reduce tracking error. In this structure, we do not need a precise reference model, and all the uncertainties are left to the UKF estimator and the compensation strategy.

In this section, we design an AME-PD control method of the bending angle α with the strategy shown in Fig. 4. With

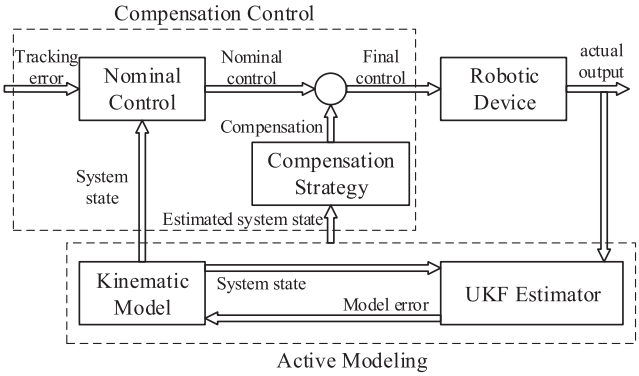

FIGURE 4. The diagram of the control strategy.

the estimator of (17), the real kinematic of scope-tip could be estimated in real time. The applied pulling velocity $\dot{\delta l}_k$ can be expressed as

$$v_{\delta l(k)} = v_{\delta lnom(k)} + v_{\delta lcom(k)} \tag{19}$$

where $v_{\delta lnom(k)}$ is the nominal control, and $v_{\delta lnom(k)}$ is the compensation designed by the compensation strategy as Fig. 4 shows. If the measurement bending angle $\tilde{\alpha}_k$ can track the target trajectory $\alpha_{d(k)}$ precisely, it obtains

$$\tilde{\alpha}_k - \alpha_{d(k)} = 0 \tag{20}$$

In this paper, the nominal input $v_{\delta lnom(k)}$ is designed by PD controller and the input compensation $v_{\delta lcom(k)}$ is designed by compensation strategy in Fig. 4. Define the tracking error of the bending angle $\alpha(k)$ as $e_k = \alpha_{d(k)} - \tilde{\alpha}_k$, and the nominal control input $v_{\delta lnom(k)}$ is

$$v_{\delta lnom(k)} = k_p e_k + k_d \frac{e_k - e_{k-1}}{T_s} \tag{21}$$

where k_p, k_d are the parameters of PD controller, thus the actual bending angle $\tilde{\alpha}_{k+1}$ is predicted to be,

$$\hat{\tilde{\alpha}}_{k+1} = \tilde{\alpha}_k + [A|v_{\delta lnom(k)}|(C\bar{\delta l}_k - \bar{\alpha}_k) + Bv_{\delta lnom(k)} + f_{h(k)}]T_s \tag{22}$$

Define the predicted tracking error

$$\hat{e}_{k+1} = \alpha_{d(k+1)} - \hat{\tilde{\alpha}}_{k+1} \tag{23}$$

In this paper, with the idea of PD controller, the predicted tracking error from (18) is calculated in the compensation strategy. Thus, the active model-based compensation is designed as

$$v_{\delta lcom(k)} = k_c \hat{e}_{k+1} \tag{24}$$

where k_c is a constant proportion parameter. Thus, the final control $v_{\delta l(k)}$ is

$$v_{\delta l(k)} = k_p e_k + k_d \frac{e_k - e_{k-1}}{T_s} + k_c \hat{e}_{k+1} \tag{25}$$

The stability of this control scheme is closely dependent on that of the normal PD control. From (23) we can see

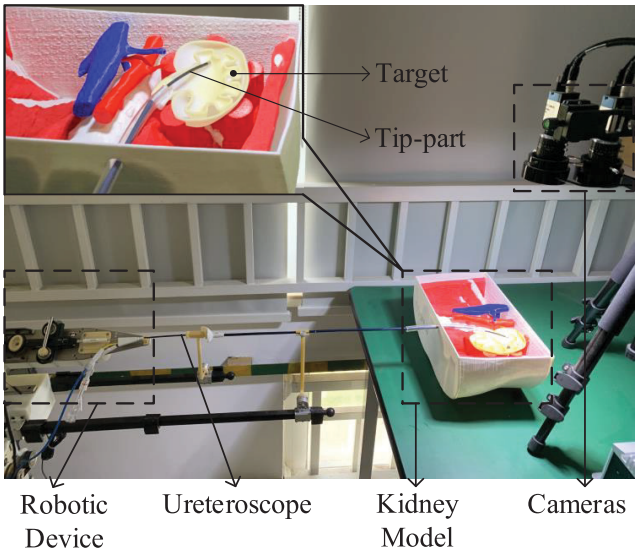

FIGURE 5. The schematic of the self-built ureteroscopy robot.

that the enhancement part is a model-predictive open loop compensation, while the $\hat{\tilde{\alpha}}_{k+1}$ is the model predictive state as (22). So, this compensation will not influence the stability of the normal PD scheme [20].

V. DEVICE SET UP AND EXPERIMENTAL ANALYSIS

A. DEVICE SET UP AND BENDING EXPERIMENTS

In this section, hardware experimental results are provided to validate the proposed scheme. The self-built robotic device held the ureteroscope and could pull or push the two rings on the handle at a given speed as shown in Fig. 5. The flexible ureteroscope operated by the robot was a 1-wire 8 F / 70 cm flexible micro-endoscope from PolyDiagnost (Lumenis, Santa Clara, CA). It composed of a single-used flexible catheter and a reusable fiber optic bundle. Two cameras (TIS GigE DFK33GP1300) were used in our experiments to measure the bending angel α of the ureteroscope. An Industrial Personal Computer (IPC, ADVANTECH ARK-3500 (Intel(R) Core(TM) i7-3610QE 2.3GHz 16.00G) served to collect data from the encoders on the robot and the cameras, and execute the control algorithms proposed.

The first experiment we conducted was to test the hysteresis of the scope. The velocity of δl was set to three constant values respectively, i.e.,

$$v_{\delta l} = \{0.125,\ 0.075,\ 0.025\}\ \text{mm/s}$$

and the experimental results were shown in Fig. 6, from which we can see there exists hysteresis clearly between the bending angle α and the wire-pulling-distance δl.

Further experiments were also conducted while the wire-pulling-velocity was set as triangular wave. The whole distance of δl was divided into three segments, i.e., $\delta l \in [0, 3]$ mm, $\delta l \in [3, 6]$ mm and $\delta l \in [0, 6]$ mm, to demonstrate the "length-dependent" hysteresis of the scope. Fig. 7 showed the results of the output of kinematic model (8) and the bending angle measurement, and Fig. 7(a), Fig. 7(b) and Fig. 7(c)

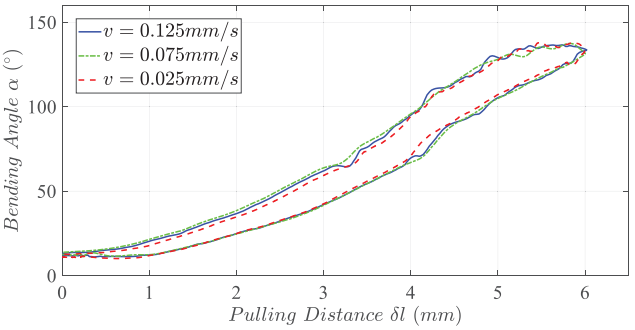

FIGURE 6. the relationship between bending angle α and the pulling distance δl.

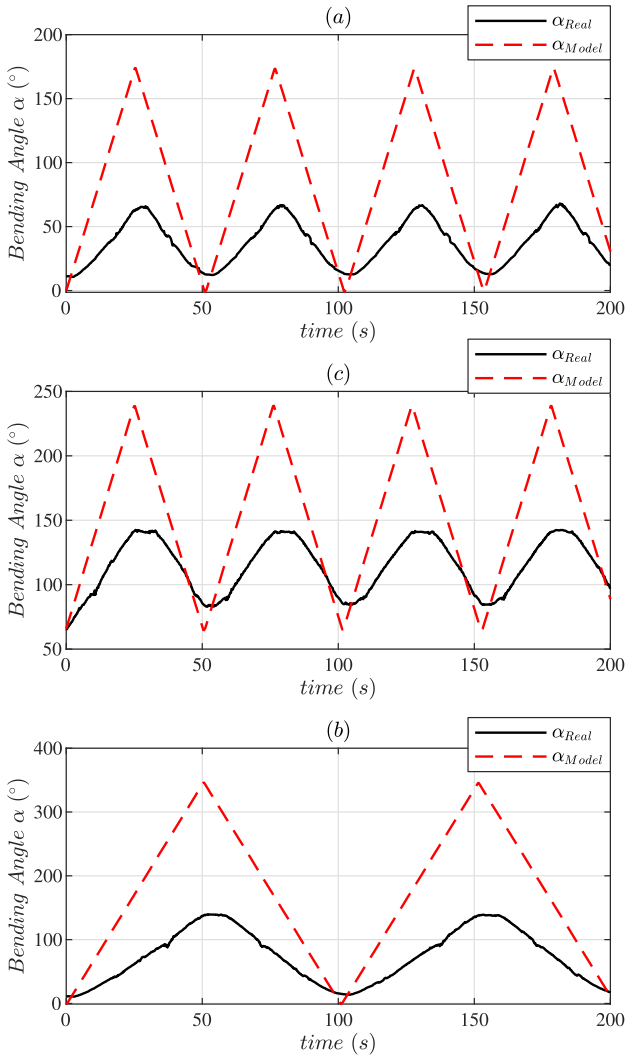

FIGURE 7. Comparison between the output of model (8) α_{Model} and the measurement of bending angle α_{Real}. (a) $\delta l \in$ [0, 3] mm; (b) $\delta l \in$ [3, 6] mm; (c) $\delta l \in$ [0, 6] mm.

were corresponding respectively to the input velocity of

$$v_{\delta l} = \begin{cases} 0.125\ \text{mm/s} & \text{when } \delta l : 0 \to 3\ \text{mm} \\ -0.125\ \text{mm/s} & \text{when } \delta l : 3 \to 0\ \text{mm} \end{cases}$$

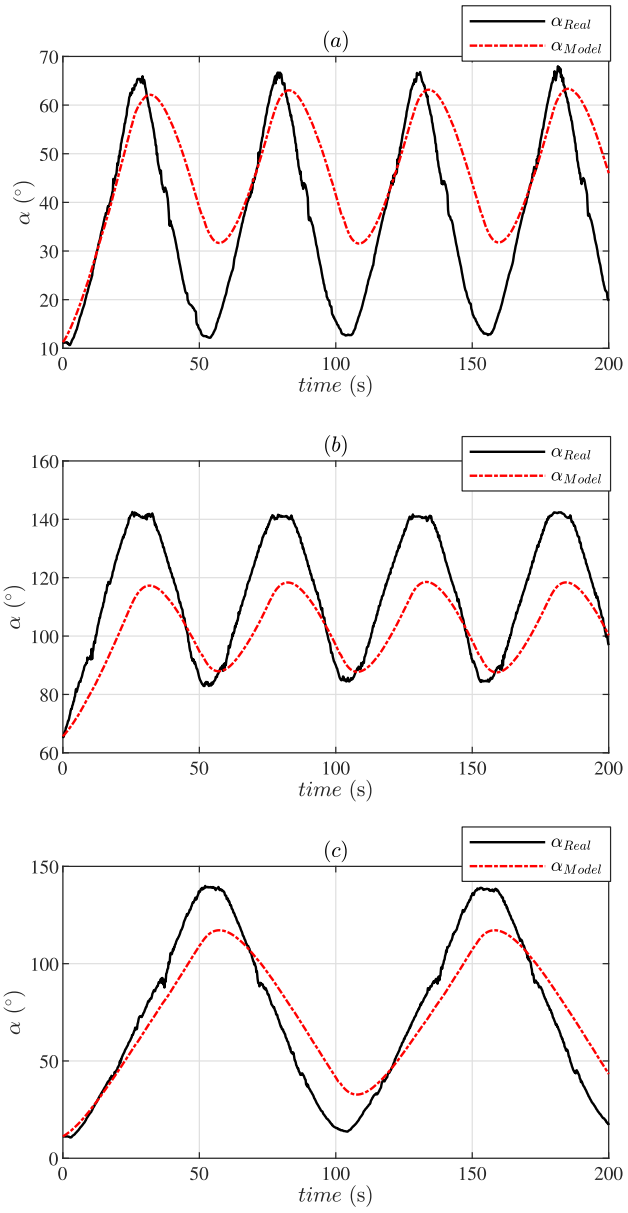

FIGURE 8. Comparison between the output of model (10) α_{Model} and the measurement of bending angle α_{Real}. (a) $\delta l \in [0, 3]$ mm; (b) $\delta l \in [3, 6]$ mm; (c) $\delta l \in [0, 6]$ mm.

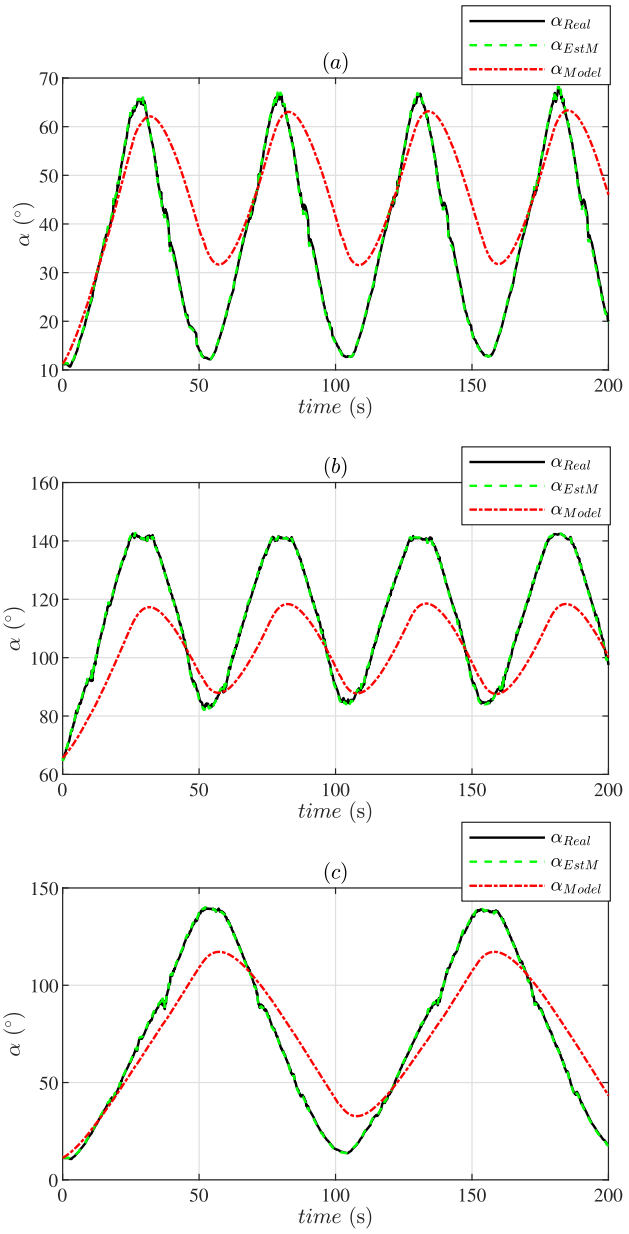

FIGURE 9. Comparison among the output of modeling error enhanced estimator α_{EstM}, the output of model (10) α_{Model}, and the measurement of bending angle α_{Real}. (a) $\delta l \in [0, 3]$ mm; (b) $\delta l \in [3, 6]$ mm; (c) $\delta l \in [0, 6]$ mm.

$$v_{\delta l} = \begin{cases} 0.125 \text{ mm/s} & \text{when } \delta l : 3 \rightarrow 6 \text{ mm} \\ -0.125 \text{ mm/s} & \text{when } \delta l : 6 \rightarrow 3 \text{ mm} \end{cases}$$

$$v_{\delta l} = \begin{cases} 0.125 \text{ mm/s} & \text{when } \delta l : 0 \rightarrow 6 \text{ mm} \\ -0.125 \text{ mm/s} & \text{when } \delta l : 6 \rightarrow 3 \text{ mm} \end{cases}$$

From Fig. 7 we can see the significant difference between them due to the influence of the unmodeled hysteresis.

B. IDENTIFICATION OF HYSTERESIS MODEL

In this study, we used genetic algorithm (GA) to identify the parameters of the A, B and C in (10). To do this, we defined the mean square error (MSE) as

$$MSE = \frac{1}{N}\sum_{i=1}^{N}(\alpha_{Real}(t) - \alpha_{Model}(t))^2 \tag{26}$$

where i is the sampling index and N is the total number of sampling points from hardware experiment, $\alpha_{Real}(t)$ is the actual bending angle measurement, $\alpha_{Model}(t)$ is the value calculated by reference model (10). The MSE is used as fitness function in GA and it represents the mean square error between measurement and the output of the model (10).

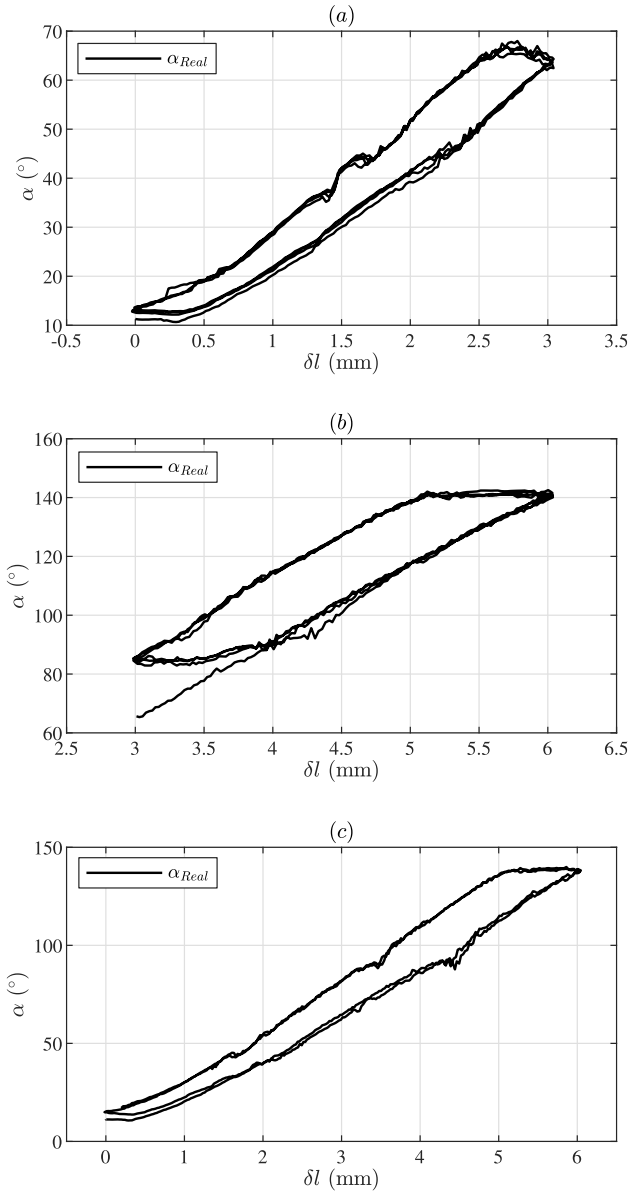

FIGURE 10. The repeatability of the measurement of bending angle α_{Real}. (a) $\delta l \in [0, 3]$ mm; (b) $\delta l \in [3, 6]$ mm; (c) $\delta l \in [0, 6]$ mm.

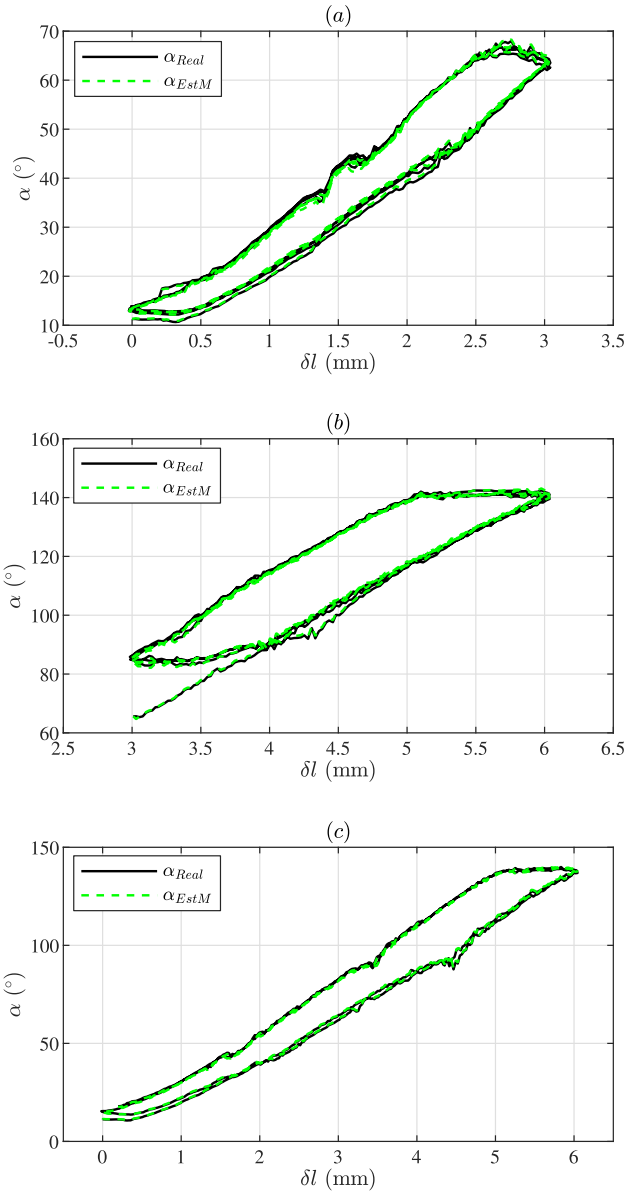

FIGURE 11. The repeatability of the output of modeling error enhanced estimator α_{EstM} and the measurement of bending angle α_{Real}. (a) $\delta l \in [0, 3]$ mm; (b) $\delta l \in [3, 6]$ mm; (c) $\delta l \in [0, 6]$ mm.

The reference model was identified using the experimental data of Fig. 7. And we got the identification results as: $[A_{Ref}, B_{Ref}, C_{Ref}] = [0.95, -0.92, 18.53]$. Fig. 8 demonstrated the results of the model output of (10) and the real measurement of α with respect to the three distance segments, where we can clearly see the modeling errors between them. Fig. 10 showed the repeatability of the nominal hysteresis model without the active estimation in different segments.

Besides the figures demonstrating the model output and the real measurements, we defined the following two indexes to quantify the errors between them.

$$Err_{Model} = \alpha_{Real} - \alpha_{Model} \tag{27}$$

$$Var_{Model} = \frac{1}{N}\sum_{i=1}^{N}[(Err_{Model(i)} - \overline{Err}_{Model})^2] \tag{28}$$

where α_{Real} and α_{Model} are the reference model output of (10) and the real measurement of the bending angle of the bending angle; $\overline{Err}_{Model}$ is the mean value of Err_{Model} and N is the number of sampling points. The Err_{Model} and Var_{Model} were calculated using the data of Fig. 8, and the results were listed in Table 2. Both Fig.8 and Table 2 prove that the reference model can only represent the tendency of the bending angle, but cannot meet the real measurement very well. The model error is clearly time varying and different when the pulling distance changes in different segments.

TABLE 2. $\overline{Err}_{Model}$ and Var_{Model} of (10) by the data of Fig.8.

δl (mm)	[0.0, 3.0]	[3.0, 6.0]	[0.0, 6.0]
$\overline{\lvert Err\rvert}_{Model}$ (deg)	11.2342	14.5564	14.9256
Var_{Model} (deg^2)	122.9452	132.4566	309.8359

TABLE 3. $\overline{Err}_{EstM}$ and Var_{EstM} of (16) by the data of Fig. 9.

δl (mm)	[0.0, 3.0]	[3.0, 6.0]	[0.0, 6.0]
$\overline{\lvert Err\rvert}_{EstM}$ (deg)	0.3270	0.4609	0.4172
Var_{EstM} (deg^2)	0.2432	0.3889	0.4123

TABLE 4. The comparison between reference model output and the results of estimation on different ranges.

δl (mm)	[0.0, 3.0]	[3.0, 6.0]	[0.0, 6.0]
$\frac{\overline{\lvert Err\rvert}_{EstM}}{\overline{\lvert Err\rvert}_{Model}}$	2.910%	3.166%	2.795%
$\frac{Var_{EstM}}{Var_{Model}}$	0.1978%	0.2936%	0.1331%

C. ACTIVE MODEL ERROR ESTIMATION

By setting the initial values as:

$$P_0 = \begin{bmatrix} 10 & 0 \\ 0 & 10 \end{bmatrix} \quad Q_0 = \begin{bmatrix} 5 & 0 \\ 0 & 15 \end{bmatrix} \quad R_0 = 0.0001 \tag{29}$$

the modeling error enhanced estimator was experimentally tested under the same scenario as that of Section V. B. Fig. 9 demonstrated the results, where we can see the errors between the estimator output and the real measurement had been reduced significantly. Fig. 11 showed the repeatability of the nominal hysteresis model with the active estimation. Two indexes were also defined as (30) and (31), and the values of Fig. 9 were calculated and listed in Table 3. Table 4 showed the ratios between the values in Table 2 and 3, which indicated the improvement achieved by the active estimation. We can see that the $\overline{|Err_{Model}|}$ has been reduced by nearly 97%, and the Var_{Model} has been reduced by more than 99.5%.

$$Err_{EstM} = \alpha_{Real} - \alpha_{EstM} \tag{30}$$

$$Var_{EstM} = \frac{1}{N}\sum_{i=1}^{N}[(Err_{EstM(i)} - \overline{Err}_{EstM})^2] \tag{31}$$

where α_{EstM} and α_{Real} are the estimated model output of (16) and real measurement of the bending angle α; $\overline{Err}_{EstM}$ is the mean value of Err_{EstM} and N is the number of sampling points.

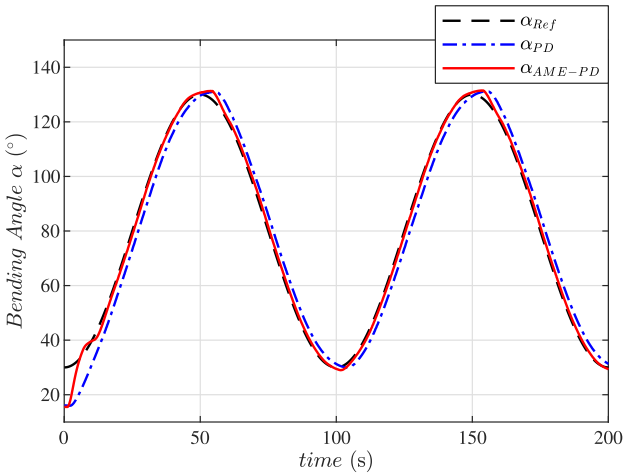

FIGURE 12. The tracking performance of bending angle by PD and AME-PD control.

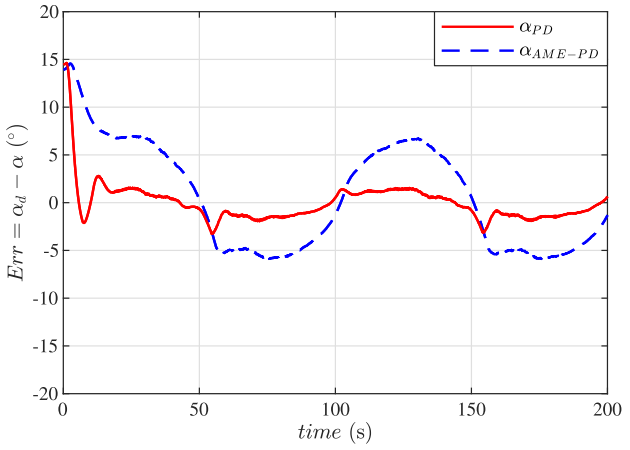

FIGURE 13. The tracking error of the PD and AME-PD control.

D. ACTIVE MODEL ENHANCED PD CONTROL

In order to test the performance of AME-PD controller designed in Section IV, the tracking trajectory $\alpha_d(t)$ is set to

$$\alpha_d(t) = -50\cos(\frac{\pi}{50}t) + 80 \tag{32}$$

the parameters of PD and AME-PD controller were set manually to $k_p = 0.02$, $k_d = 0.05$, $k_c = 0.06$, in the goal of achieving fast and accurate response. The tracking performance under the PD control and the AME-PD control were presented in Fig. 12, and the tracking errors were plotted in Fig. 13. Again, we defined the two index as:

$$Err = \alpha_{d(k)} - \tilde{\alpha}_k \tag{33}$$

$$Var = \frac{1}{N}\sum_{i=1}^{N}[(Err_i - \overline{Err})^2] \tag{34}$$

where $\alpha_{d(k)}$ and $\tilde{\alpha}_k$ are the discrete form of $\alpha_d(t)$ and $\tilde{\alpha}_k$ measured by visual capture. $\overline{Err}$ is the mean value of tracking error Err, and N is the number of sampling points.

TABLE 5. The comparison between $\overline{|Err|}$ and *Var* of the tracking error of the PD and AME-PD control.

Index	PD Controller	AME-PD Controller	AME-PD/PD
$\overline{\lvert Err \rvert}$	5.0535	1.3424	26.56%
Var	30.8419	4.0311	13.07%

The corresponding values were listed in Table 5, where we can see that the tracking error had been improved by more than 70% after introducing the simple ''estimator predictive enhancement'' of k_c into (24).

VI. CONCLUSION

In this paper, the active modeling scheme, which is composed of the Coleman-Hodgdon backlash model and the UKF-based model error estimation, was proposed for the robotic flexible ureteroscopy. This intended to obtain an accurate description, and also a compensation control of the hysteresis of the flexible scope. Compared with the existed methods such as the hysteresis model with adaptive parameters, the proposed scheme might be more feasible for real implementation. Besides the simple structure and good performance we had shown, the UKF-based active estimation is a kind of 'data-driven', and the Kalman Filter type algorithm has been extensively applied on real systems and its robustness and feasibility have been verified.

In additional to the flexible ureteroscopy we had tested, the proposed scheme might be a general approach for the active modeling and tracking control of other flexible scopes. And besides the simple PD-type ''active model predictive'' compensation introduced in this paper, a nonlinear control was under design and test for near future publication.

ACKNOWLEDGMENT

(Dongyang Bie is co-first author.)

REFERENCES

[1] L. C. Zhao, A. C. Weinberg, Z. Lee, M. J. Ferretti, H. P. Koo, M. J. Metro, D. D. Eun, and M. D. Stifelman, ''Robotic ureteral reconstruction using buccal mucosa grafts: A multi-institutional experience,'' *Eur. Urol.*, vol. 73, no. 3, pp. 419–426, Mar. 2018.

[2] X. Li, A. M. H. Tiong, L. Cao, W. Lai, P. T. Phan, and S. J. Phee, ''Deep learning for haptic feedback of flexible endoscopic robot without prior knowledge on sheath configuration,'' *Int. J. Mech. Sci.*, vol. 163, Nov. 2019, Art. no. 105129.

[3] J. Burgner-Kahrs, D. C. Rucker, and H. Choset, ''Continuum robots for medical applications: A survey,'' *IEEE Trans. Robot.*, vol. 31, no. 6, pp. 1261–1280, Dec. 2015.

[4] H.-S. Yoon, J. H. Jeong, and B.-J. Yi, ''Image-guided dual master–slave robotic system for maxillary sinus surgery,'' *IEEE Trans. Robot.*, vol. 34, no. 4, pp. 1098–1111, Aug. 2018.

[5] S. Y. Nakada and M. S. Pearle, *Advanced Endourology: The Complete Clinical Guide*. Cham, Switzerland: Springer, 2007.

[6] B. Yi, G. Wang, J. Li, J. Jiang, Z. Son, H. Su, and S. Zhu, ''The first clinical use of domestically produced Chinese minimally invasive surgical robot system 'Micro Hand S,''' *Surgical Endoscopy*, vol. 30, no. 6, pp. 2649–2655, 2016.

[7] R. Saglam, A. Y. Muslumanoglu, Z. Tokatlı, T. Çaşkurlu, K. Sarica, A. I. Taşçi, B. Erkurt, E. Süer, A. S. Kabakci, G. Preminger, O. Traxer, and J. J. Rassweiler, ''A new robot for flexible ureteroscopy: Development and early clinical results (IDEAL stage 1–2b),'' *Eur. Urol.*, vol. 66, no. 6, pp. 1092–1100, 2014.

[8] R. J. Webster and B. A. Jones, ''Design and kinematic modeling of constant curvature continuum robots: A review,'' *Int. J. Robot. Res.*, vol. 29, no. 13, pp. 1661–1683, Nov. 2010.

[9] L. Ott, F. Nageotte, P. Zanne, and M. de Mathelin, ''Robotic assistance to flexible endoscopy by physiological-motion tracking,'' *IEEE Trans. Robot.*, vol. 27, no. 2, pp. 346–359, Apr. 2011.

[10] A. Hooshiar, S. Najarian, and J. Dargahi, ''Haptic telerobotic cardiovascular intervention: A review of approaches, methods, and future perspectives,'' *IEEE Rev. Biomed. Eng.*, vol. 13, pp. 32–50, Apr. 2020.

[11] T. N. Do, T. Tjahjowidodo, M. W. S. Lau, and S. J. Phee, ''Nonlinear friction modelling and compensation control of hysteresis phenomena for a pair of tendon-sheath actuated surgical robots,'' *Mech. Syst. Signal Process.*, vols. 60–61, pp. 770–784, Aug. 2015.

[12] T. N. Do, T. Tjahjowidodo, M. W. S. Lau, T. Yamamoto, and S. J. Phee, ''Hysteresis modeling and position control of tendon-sheath mechanism in flexible endoscopic systems,'' *Mechatronics*, vol. 24, no. 1, pp. 12–22, Feb. 2014.

[13] T. N. Do, T. Tjahjowidodo, M. W. S. Lau, and S. J. Phee, ''An investigation of friction-based tendon sheath model appropriate for control purposes,'' *Mech. Syst. Signal Process.*, vol. 42, nos. 1–2, pp. 97–114, Jan. 2014.

[14] J. Li, G. Zhang, Y. Xing, H. Liu, and S. Wang, ''A class of 2-degree-of-freedom planar remote center-of-motion mechanisms based on virtual parallelograms,'' *J. Mech. Robot.*, vol. 6, no. 3, Aug. 2014, Art. no. 031014.

[15] J. Li, S. Wang, X. Wang, and L. Zhang, ''Setup optimization for MIS robots with two-passive joints,'' in *Proc. IEEE Int. Conf. Robot. Autom.*, May 2011, pp. 2418–2423.

[16] L. A. Zhang, R. Khare, E. Wilson, S. X. Wang, C. A. Peters, and K. Cleary, ''Robotic assistance for manipulating a flexible endoscope,'' in *Proc. IEEE Int. Conf. Robot. Autom. (ICRA)*, May 2014, pp. 5380–5385.

[17] J. Legrand, M. Ourak, A. Javaux, C. Gruijthuijsen, M. A. Ahmad, B. Van Cleynenbreugel, T. Vercauteren, J. Deprest, S. Ourselin, and E. V. Poorten, ''From a disposable ureteroscope to an active lightweight fetoscope–characterization and usability evaluation,'' *IEEE Robot. Autom. Lett.*, vol. 3, no. 4, pp. 4359–4366, Oct. 2018.

[18] B. D. Coleman and M. L. Hodgdon, ''A constitutive relation for rate-independent hysteresis in ferromagnetically soft materials,'' *Int. J. Eng. Sci.*, vol. 24, no. 6, pp. 897–919, Jan. 1986.

[19] D. Zhang, X. Zhao, and J. Han, ''Active model-based control for pneumatic artificial muscle,'' *IEEE Trans. Ind. Electron.*, vol. 64, no. 2, pp. 1686–1695, Feb. 2017.

[20] S. Schaller, J. Lippert, L. Schaupp, T. R. Pieber, A. Schuppert, and T. Eissing, ''Robust PBPK/PD-based model predictive control of blood glucose,'' *IEEE Trans. Biomed. Eng.*, vol. 63, no. 7, pp. 1492–1504, Jul. 2016.

XIANGYU WANG (Student Member, IEEE) was born in Hebei, China. He received the B.E. degree in intelligent science and technology from Nankai University, Tianjin, China, in 2017. He is currently pursuing the Ph.D. degree in control science and engineering with the Institute of Robotics and Automatic Information Systems, Nankai University, Tianjin, China.

His main research interests include nonlinear estimation and control, robotics, and pattern recognition.

DONGYANG BIE was born in Henan, China. He received the Ph.D. degree in mechatronic engineering from the Harbin Institute of Technology, Harbin, China, in 2018.

He is currently a Lecturer with the Institute of Robotics and Automatic Information Systems, Nankai University, Tianjin, China. His research interests include multi-agent systems and medical robotics.

JIANDA HAN (Member, IEEE) was born in Liaoning, China, in 1968. He received the Ph.D. degree in mechatronic engineering from the Harbin Institute of Technology, Harbin, China, in 1998.

From 1998 to 2003, he was a Visiting Scientist with the City University of Hong Kong, Hong Kong; Michigan State University, East Lansing, MI, USA; and Cornell University, Ithaca, NY, USA. He is currently a Professor with the Institute of Robotics and Automatic Information Systems, Nankai University, Tianjin, China. His research interests include nonlinear estimation and control, robotics, and mechatronics systems.

YONGCHUN FANG (Senior Member, IEEE) was born in Hunan, China, in 1973. He received the B.S. and M.S. degrees in control theory and applications from Zhejiang University, Hangzhou, China, in 1996 and 1999, respectively, and the Ph.D. degree in electrical engineering from Clemson University, Clemson, SC, USA, in 2002.

From 2002 to 2003, he was a Postdoctoral Fellow with the Sibley School of Mechanical and Aerospace Engineering, Cornell University, Ithaca, NY, USA. He is currently a Professor with the Institute of Robotics and Automatic Information Systems, Nankai University, Tianjin, China. His research interests include nonlinear control, visual servoing, control of underactuated systems, and AFM-based nanosystems.